# Vesiculation in rhyolite at low $H_2O$ contents: A thermodynamic model

Amy G. Ryan

James K. Russell

Kai-Uwe Hess[a]

A.B. Phillion[b]

and

Donald B. Dingwell[a]

Centre for Experimental Studies of the Lithosphere
Earth, Ocean and Atmospheric Sciences
University of British Columbia
Vancouver, Canada V6T 1Z4

[a]Earth & Environmental Sciences, Ludwig Maximilian University, 80333 Munich, Germany
[b]School of Engineering, University of British Columbia, Kelowna, Canada V1V 1V7

**Geochemistry, Geophysics, Geosystems**
**REVISION 1**
**November 3, 2015**

*Corresponding Author: J.K. Russell [krussell@eos.ubc.ca; +1-778-995-7710]

## Key Points

- High-T experiments reveal kinetics of bubble nucleation and growth in rhyolite
- XCT gives bubble numbers and size distributions at experimental conditions
- Vesiculation in rhyolite is modeled using chemical affinity and melt viscosity

# Abstract

We present experimental data on the thermodynamics and kinetics of bubble nucleation and growth in weakly $H_2O$-oversaturated rhyolitic melts. The high-temperature (900-1100°C) experiments involve heating of rhyolitic obsidian from Hrafntinnuhryggur, Krafla, Iceland to above their glass transition temperature ($Tg$ ~ 690°C) at 0.1 MPa for times of 0.25-24 hours. During experiments, the rhyolite cores increase in volume as $H_2O$ vapour-filled bubbles nucleate and expand. The extent of vesiculation, as tracked by porosity, is mapped in temperature-time ($T$-$t$) space. At constant temperature and for a characteristic dwell time, the rhyolite cores achieve a maximum volume where the $T$-$t$ conditions reach thermochemical equilibrium. For each *T-t snapshot* of vesiculation, we use 3D analysis of X-ray computed tomographic (XCT) images of the quenched cores to obtain the bubble number density (BND) and bubble size distribution (BSD). BNDs for the experimental cores are insensitive to $T$ and $t$, indicating a single nucleation event. All BSDs converge to a common distribution, independent of $T$, melt viscosity ($\eta$), or initial degree of saturation, suggesting a common growth process. We use these data to calibrate an empirical model for predicting the rates and amounts of vesiculation in rhyolitic melts as a function of $\eta$ and thermochemical affinity ($A$): two computable parameters that are dependent on $T$, pressure and $H_2O$ content. The model reproduces the experimental dataset and data from the literature to within experimental error, and has application to natural volcanic systems where bubble formation and growth are not diffusion limited (e.g., lavas, domes, ignimbrites, conduit infill).

## 1. Introduction

The rates and extents of vesiculation in natural silicate melts govern the behaviour of volcanic systems by controlling the potential energy stored within the magma to the point of eruption and, thereby, dictating eruption style (explosive vs. effusive). In silicic volcanic systems the forms of effusive eruption (e.g., dome, spine or lava) are commonly ascribed to variations in the rheological properties of the magma [e.g., *Bagdassarov et al.,* 1996; *Mader et al.,* 2013]. Rheological properties, in turn, are strongly influenced by the concentrations of dissolved and exsolved magmatic volatiles, particularly $H_2O$ [e.g., *Giordano et al.,* 2008; *Pistone et al.,* 2013; *Vona et al.,* 2013]. Nowhere is the sensitivity of melt and magma viscosity to $H_2O$ contents more apparent than at relatively low concentrations. At these conditions, slight changes in the amounts of dissolved or exsolved $H_2O$ contents can cause significant changes in the melt rheology [*Hess and Dingwell,* 1996; *Giordano et al.,* 2008; *Quane et al.,* 2009]. On this basis, the timescales of volatile exsolution and vesiculation processes in weakly oversaturated silicic magma systems represent critical elements for understanding the controls on effusive eruption styles [e.g., *Bagdassarov et al.,* 1996; *Navon et al.,* 1998].

Exsolution of a fluid phase from oversaturated melts involves nucleation and growth of bubbles. The processes of bubble nucleation and growth in silicate melts have been studied from a variety of perspectives, including: high-temperature ($T$) experimentation [e.g., *Hurwitz and Navon*, 1994; *Bagdassarov et al.,* 1996; *Lyakhovsky et al.*, 1996; *Navon et al.,* 1998; *Gardner et al.,* 2000; *Larsen and Gardner*, 2000; *Mourtada-Bonnefoi and Laporte,* 2004; *Gardner and Ketcham,* 2011], theoretical modelling [e.g., *Sparks,* 1978; *Toramaru,* 1989, 1995; *Proussevitch and Sahagian,* 1998; *Blower et al.,* 2001; *Lensky et al.,* 2004; *L'Heureux,* 2007; *Gonnermann and Gardner,* 2013; *Huber et al.,* 2014], and inversion of field-based observations [e.g., *Gaonac'h et al.,* 1996; *Mangan and Cashman,* 1996; *Castro et al.,* 2005; *Giachetti et al.*, 2010;

*Watkins et al.,* 2012]. These studies have elucidated a diversity of competing processes and rates inherent in the vesiculation process.

Experimental studies of bubble nucleation and growth dynamics in natural silicate melts have mainly relied on depressurization events of 10's to 100's of MPa applied to $H_2O$ oversaturated melts held at elevated pressures and temperatures [e.g., *Hurwitz and Navon,* 1994; *Lyakhovsky et al.,* 1996; *Gardner et al.,* 2000; *Mangan and Sisson,* 2000; *Lensky et al.,* 2004; *Mourtada-Bonnefoi and Laporte,* 2004; *Baker et al.,* 2006; *Hamada et al.,* 2010; *Gardner and Ketcham,* 2011; *Gonnermann and Gardner,* 2013; *McIntosh et al.,* 2014; *Martel and Iacono-Marziano,* 2015; *Marxer et al.* 2015]. In these experiments, decompression rapidly moves the melt from undersaturated or saturated states to oversaturation, where bubble nucleation and growth operate far from chemical equilibrium. Under these conditions nucleation is often limited to a single event [e.g., *Lyakhovsky et al.,* 1996; *Gardner et al.,* 1999; *Mourtada-Bonnefoi and Laporte,* 2004; *Baker et al.,* 2006]. Such experiments have shown bubble growth to be complexly related to melt viscosity, volatile diffusion rate, and the number of bubbles present [e.g., *Lyakhovsky et al.,* 1996; *Navon et al.,* 1998; *Gardner et al.,* 1999; *Larsen and Gardner,* 2000; *Lensky et al.,* 2004]. The observed bubble nucleation and growth rates in these experiments have been used to map equilibrium and disequilibrium degassing regimes as a function of intrinsic and extrinsic properties of the system (e.g., $T$, viscosity, % crystals, volatile content, and decompression rate) [e.g., *Hurwitz and Navon,* 1994; *Lyakhovsy et al.,* 1996; *Gardner et al.,* 1999; *Mangan and Sisson,* 2000; *Lensky et al.,* 2004; *Mourtada-Bonnefoi and Laporte,* 2004; *Burgisser and Gardner,* 2005; *Martel and Iacono-Marziano,* 2015]. Lastly, these experiments also provide insight into the conditions and time-scales for bubble coalescence and permeability formation [e.g., *Larsen et al.,* 2004; *Burgisser and Gardner,* 2005; *Gardner,* 2007a; *Castro et al.,* 2012; *Martel and Iacono-Marziano,* 2015].

An alternative experimental approach involves the *in situ* or time-dependent measurement of bubble growth at high-*T* and at elevated *P* (e.g., 300-2200 MPa [*Martel and Bureau*, 2001; *Gonde et al.*, 2011]) or at atmospheric conditions [e.g. *Bagdassarov et al.*, 1996; *Stevenson et al.*, 1997; *Navon et al.*, 1998; *Liu and Zhang*, 2000; *Bai et al.*, 2008; *Baker et al.*, 2012; *Fife et al.*, 2012; *Masotta et al.*, 2014]. The main advantage of these studies is that they provide information on the time-dependent paths of bubble formation and growth, as well as, the end-state of the growth process. These data can be used directly to constrain the fundamental physics of the nucleation, growth and vesiculation processes, and to develop and test existing models.

Here we present a new suite of high-*T* (>*Tg*), low-*P* (0.1 MPa) foaming experiments on cores of weakly oversaturated natural rhyolitic glass designed to inform on vesiculation during lava effusion. We use high-resolution X-ray computed tomography (XCT) to recover bubble population statistics for each experiment including bubble number and size distributions. These data are used to interrogate the dataset for changes in the nucleation and/or growth dynamics with increasing time or temperature. Additionally, these data provide *snapshots* of porosity development over fixed amounts of time at constant *T*, thereby constraining the kinetics and thermodynamics of vesiculation processes in lavas. Lastly, we use the experimental data to create a predictive model for vesiculation (e.g., rates and volumes) as a function of the thermodynamic potential for fluid exsolution (i.e., chemical affinity, *A*) and the viscosity of the melt.

## 2. Materials

### 2.1 Starting material

The starting material for this study is fresh rhyolitic obsidian from Hrafntinnuhryggur, Krafla, Iceland donated by Hugh Tuffen (pers. comm. 2008). The glass is essentially bubble- and crystal-free, texturally homogeneous (Fig. 1), and has been described and chemically analyzed by Tuffen and Castro [2009]. Table 1 reports the anhydrous chemical composition of the obsidian block used in these experiments as measured by electron microprobe [*Tuffen and Castro,* 2009] and X-ray fluorescence analyses. $H_2O$ is the only volatile present and the $H_2O$ content measured by Fourier transform infrared spectroscopy (FTIR) is 0.11(4) wt.%. At 0.1 MPa and temperatures in excess of 900°C the initial $H_2O$ content of the glass is 5-15% greater than the modeled $H_2O$ solubility limit [*Ryan et al.,* 2015].

The use of this starting material for study of the formation and growth of $H_2O$-filled bubbles in silicic melts is opportunistic. The remarkable textural and chemical homogeneity of the glass, the low $H_2O$ content, the absence of other volatile species [cf. *Bagdassarov et al.,* 1996; *Stevenson et al.*, 1997], combined with the tendency of the glass cores to behave as closed systems (see below), make this an ideal material for these experiments.

### *2.2 Vesiculation experiments and results*

A total of 33 high-*T* vesiculation experiments were performed on cores of natural obsidian (Table 2). Ryan et al. [2015] fully describe the experimental method. Each experiment used a 10 x 10 mm cylindrical obsidian core of known mass and volume; the cores were placed on a preheated ceramic base in a Nabertherm HTC 08/15 furnace and held at temperatures between 900-1100°C for dwell times of 15 minutes to 24 hours. Modelling pure heat conduction indicates the interior of the core reaches *T* greater than the measured calorimetric glass transition temperature of the melt (*Tg* ~690 ± 20°C [*Castro et al.,* 2008]) in <1 min, and the final experimental *T* in <2-5 min. After reaching the appropriate dwell time the ceramic base and obsidian core were removed from the furnace and quenched below *Tg* in <10 seconds without any observable modification to the shape and volume of the core. The final mass and volume of the foamed cores were then measured using a high precision balance (σ ± 0.006 mg) and a Micromeritics AccuPyc II 1340 helium pycnometer (σ ± 0.04%), respectively. The propagated uncertainty in calculated values of porosity is 1.38% and is corroborated by replicate measurements.

During the isothermal experiments, sample volume increases with time (Fig. 1) until it stabilizes at a maximum value ('plateau samples'). Ryan et al. [2015] interpreted the increase in sample volume to be the $H_2O$-oversaturated system exsolving excess dissolved volatiles (e.g., $H_2O$), thereby inducing bubble nucleation and growth. Plateau samples mark the cessation of exsolution and bubble growth, indicating that the equilibrium concentration of $H_2O$ for that temperature at 0.1 MPa has been reached. The volume of the plateau samples and the rate at which this volume is achieved increases with increasing temperature. There is no evidence for bubble nucleation on the exterior surfaces nor for fluid escape from the core suggesting that each core behaves as a closed system over the timescale of the experiments. Collectively, the experimental products provide *snapshots* of vesiculation and, thus, bubble populations in time-temperature space.

Of the 33 cores produced in the high-temperature vesiculation experiments, 22 were selected for X-ray computed tomography analysis (Table 2). Four other samples of varying porosity (starting material: 0%, AR-IK-10: 18.3%, AR-IK-11: 57.4%, AR-IK-16: 66.7%) were thin-sectioned and selected for 2D imaging by scanning electron microscopy (SEM) using a Philips XL-30 Scanning Electron Microscope at the University of British Columbia. These 2D images were used as reference materials to verify 3D image analysis results (Supporting Information Text S1).

## 3. Methods

### *3.1 3D image acquisition*

Three-dimensional high-resolution images at a voxel size of 18.5 µm were acquired using a GE phoenix® v|tome|x s 240 micro-CT scanner partially owned by Mineralogy and Petrology at the Department of Earth and Environmental Sciences of the LMU Munich and housed at the Institute of Medical Engineering of the Technical University of Munich (IMETUM). For each scan, 1000 radiographs, scanning 360°, were acquired at an exposure time of 333 ms using a voltage of 80 kV, a current of 130 µA, and a 0.2 mm VA-steel filter. The resulting set of XCT radiographs was then reconstructed using the inverse radon transformation [*Deans,* 2007] to generate a 3D image (990 x 990 x 1000 voxels, at 16-bit greyscale) of the internal structure of the vesicular glass cores.

### *3.2 Image analysis*

The XCT datasets were analyzed using the ImageJ 1.47v [*Schneider et al.,* 2012] and Avizo® Fire (v.8) programs in order to characterize the bubble populations in the obsidian cores (Supporting Information Text S2). The image contrast in the original 3D reconstructed datasets was adjusted using ImageJ to make solid materials nearly white and air nearly black. This parameter was increased only to the point where noise was removed without marked change to bubble shape and size. In Avizo® Fire, a greyscale threshold was applied to the contrast-enhanced set of greyscale images to binarize the datasets, and to identify the bubbles as the entity of interest. Neighboring bubbles were separated using a watershed algorithm, which identifies gradients based on a distance transform (the ‘Separate Objects’ command in Avizo® Fire). This process effectively reconstructs bubble walls that fall below the resolution limit of the XCT imaging process. Each separated bubble was then labeled, counted, and characterized in terms of its volume. A similar process was applied to the glass phase to collect volume data for the glass in the cores ($V_G$; Table 2).

### *3.3 Data treatment and sources of error*

We identify two potential artifacts in the imaging process. The first, Type A, occurs when greyscale-thresholding accidently separates voxels from the entity to which they belong, overestimating the number of small entities in the core. To eliminate Type A artifacts we used 2D image analysis of high-magnification SEM images for 3 samples (AR-IK-10, AR-IK-11, and AR-IK-16) to identify and measure the smallest bubbles present (Fig. A1). In each sample the smallest bubbles have radii of ~25 μm. The volume of a sphere having this minimum radius (~65450 $\mu m^3$; ~10 voxels) was then used to truncate the raw bubble size data [e.g., *Phillion et al.*, 2008].

The second potential artifact related to imaging, Type B, results from an image analysis program artificially and erroneously lumping separate entities together. This occurs when the glass film between bubbles is less than the resolution of the 3D dataset. We eliminated these artifacts by using ImageJ to manually examine each stack of 2D images to identify and measure the radius of the largest bubble, often a distinct outsized bubble. The volume of a sphere with that maximum radius was then used as the limit for accurate bubble size data in that sample. Using these data treatment processes we overcame most resolution-related artifacts, and recovered the bubble size distribution and approximate bubble number within each core. The maximum reduction in the porosity of a core as a result of data truncation is 1.2%. Select datasets are available in Supporting Information (Data Sets S1-S9).

Two samples, one each of low (AR-IK-32) and high (AR-IK-23) porosity, were reprocessed *ab initio* to check the user's ability to pick the same parameters for enhancing the image contrast and to select the same binarizing threshold. Calculated porosities for these samples (AR-IK-32, AR-IK-23) have standard deviations of <5% porosity (Fig. 2a).

## 4. Results

### 4.1 Porosity

Each core imaged by XCT was processed separately to obtain estimates of the bubble population (number and size) and the volume of framework glass. The porosity of the core at the end of the experiment is taken as the ratio of bubble volume ($V_B$) to the volume sum of the glass and the bubbles as measured in Avizo® Fire ($\phi_{AF}$; Table 2). In our analysis of the experimental data we assume that volume expansion of the sample results only from bubble formation and expansion and that thermal expansion of the melt can be neglected. This assumption is reasonable given that the maximum volume change predicted from the melt being heated to 1100°C is 0.65% [*Bagdassarov and Dingwell*, 1992], which is within our measurement uncertainty for porosity (1.38%). Figure 2a shows values of $\phi_{AF}$ calculated by image analysis compared to values from core volumes measured by He-pycnometry ($\phi_{HP}$). The data are distributed along the 1:1 line (Fig. 2a) indicating good agreement between the two different methods.

Figure 2b shows the changes in $\phi$ for samples within suites of experiments performed at the same temperature (hereafter referred to as a *T*-suite). The experimental uncertainty in $\phi$ based on replicate experiments (same *T* and similar *t*) varies between 2.5-8.0% porosity and is inversely proportional to $\phi$. Our largest uncertainties are in the 900°C suite at conditions where $\phi<25\%$ (t~12.5 h) (Table 2). In each *T*-suite, $\phi$ increases with time until it reaches a maximum plateau value. After reaching this plateau value, values of $\phi$ decrease slightly in experiments having very long dwell times (Fig. 2b; end-points in each *T*-suite). This decrease in $\phi$, also expressed by a slight sagging of the core (Fig. 1), ensures the plateau value is indeed a maximum. The sagging occurs where the timescale of the experiment begins to compete with the relaxation timescale of the bubbly-melt at high-$T$. The plateau value of $\phi$ increases with increasing $T$ and is an expression of $H_2O$ retrograde solubility [*Ryan et al.*, 2015]. The slope of the initial curved portion of each trend line is the initial rate of change in sample volume, which increases with increasing temperature (Fig. 2b). This positive correlation between vesiculation rate and temperature is a first indication that a $T$-dependent property of the melt (i.e. viscosity) governs the rate, and thus kinetics, of vesiculation in this system.

### *4.2 Bubble number density (BND)*

Bubble number density is a normalized measure of the number of bubbles in a sample, and is calculated by dividing the total number of bubbles ($n_B$) by the volume of the melt taken as the initial volume (mm$^{-3}$) of the core ($V_i$) [*Proussevitch et al.*, 2007]. BND values for each experiment are reported in Table 2 and vary between $5 < \mathrm{BND} < 30$ mm$^{-3}$. Within each $T$-suite, BND shows no clear pattern with increasing time. Similarly, BND does not vary systematically with increasing $T$ (Table 2).

### *4.3 Bubble size distribution (BSD)*

Bubble size distributions are illustrated against bubble radius in two ways: cumulative bubble volume fraction ($\Sigma V$) (Fig. 3a-c), and cumulative number fraction of bubbles greater than a radius '$r$' per mm$^3$ of melt ($\Sigma N(>r)$) (Fig. 3d-f; cf. *Gaonac'h et al.*, 1996; *Blower et al.*, 2002; *Shea et al.*, 2010). There are three apparent changes in BSDs with increasing $\phi$. Firstly, there is a systematic shift of the curves to the right as porosity rises to ~40% (Fig. 3a,b), indicating a decrease in the volume contribution of smaller ($r$ = 25-200 μm) bubbles. Secondly, there is a general increase in the size and proportions of the largest bubbles, from a maximum of 500 μm below 20% porosity to 1500 μm in a sample above 60% porosity. Thirdly, there is tremendous similarity in the slope and location of BSDs once the samples reach porosities ≥ 40%; 200-500 μm sized bubbles volumetrically dominate the BSD. A final more subtle feature of the BSD curves is the overall increase in the slope of the curves with increasing porosity to a maximum at ~60-75% (Fig. 3c). The increase in the slope of the curve is analogous to an increase in degree of sorting ascribed to grain size distribution curves (i.e., $r_\sigma$ [*Cas and Wright,* 1987]) and indicates a tighter range in the volumetrically dominant bubble size.

The BSDs are shown as a function of time for specific *T*-suites in Fig 3(d-f). In each *T*-suite the shape of curve shifts at $\phi > 40\%$: below 40% curves are concave-down, have short horizontal plateaus at small bubbles sizes, and decrease smoothly to maximum values from 300 to 500 μm, indicating numerous bubbles in small size fractions (<200 μm). At porosities > 40%, both, the density of small bubbles and the variance in the size range of the larger bubbles decrease. This is expressed as a prominent horizontal plateau that terminates at ~200 μm to become a nearly vertical curve terminating at maximum bubble sizes of 400-1000 μm. In each isothermal suite (Fig. 3d-f) the strongly curved portion of the BSD moves right with *t* to nearly the same position marked by a nearly vertical slope (e.g., 2.5, 5, 20 and 24 h curves in the 925°C suite (Fig. 3d)).

Lastly, Figure 4 shows BSDs and 2D cross-sections of the 3D XCT images for plateau samples (cf. solid black lines in Fig. 3d-f). The BSD curves for these plateau samples are similar regardless of *T*. This similarity indicates that although the *T*-dependent $H_2O$ solubility controls the total amount of volatile exsolved, the final bubble sizes and distributions are *T*-independent. One would expect, given the strong *T*-dependence of the maximum porosity value, that there should be a sympathetic *T*-dependence for BSDs or BNDs. However we cannot discern such a pattern from our data. The change in $\phi$ with $T$ could therefore be the result of subtle changes in either or both of these parameters with increasing $T$.

Bubble-free rinds separate the surface of each core from its vesicular interior (Fig. 4). These rinds are present in all samples and comprise 3-7% of the total core volume; within each $T$-suite the rind thicknesses increase with time. von Aulock et al. [2015] also observed formation and progressive thickening of an impermeable skin on foaming obsidian samples, and ascribe skin formation to diffusional loss of water from the surface, as well as surface tension driven bubble collapse. We attribute the rinds in these experiments to small amounts of diffusive water loss from the surfaces of the samples during the high-$T$ experiment. The maximum diffusion length scale ($L_D$) in plateau samples is 0.15-0.43 mm (where $L_D = (4\ D\ \tau_{eq})^{0.5}$ [*Crank,* 1975]). This length scale is of the same magnitude as the maximum observed bubble-depleted rind in the dataset (0.4 mm; Table 3). Ryan et al. [2015] modeled the maximum diffusive $H_2O$ loss to be approximately 0.37 mg after 20 hours of exposure to high temperatures, which has a negligible effect on the overall concentration of $H_2O$ dissolved in the melt. However a viscosity contrast up to 0.5 log units [*Giordano et al.,* 2008] may arise if the dehydration of the rind is complete. This potential viscosity contrast could affect the overall rheology of the sample and may explain why bubbles are unable to penetrate the exterior surfaces and escape the cores.

## 5. Bubble nucleation and growth

Our BND values vary from 6 to 30 mm$^{-3}$ across the entire dataset and do not change systematically with $T$. The variance in the dataset is similar to previous studies of bubble nucleation in silicate melts but BND values are 1-3 orders of magnitude lower than those produced by decompression experiments [*Hurwitz and Navon,* 1994; *Gardner et al.,* 2000; *Gardner and Denis,* 2004; *Baker et al.,* 2006; *Gardner,* 2007b; *Nowak et al.,* 2011; *Gonnermann* *and Gardner,* 2013]. Mangan and Sisson [2000], Gardner and Denis [2004] and Gonnermann and Gardner [2013] previously documented a positive relationship between BND and supersaturation pressure and, on that basis, we ascribe our lower BND values to the differences in degree of $H_2O$ supersaturation in our study and the high degrees of supersaturation characteristic of depressurization experiments. Within our dataset the modest differences in the supersaturation state of samples are insufficient to affect BND values. Within individual *T*-suites, BND values vary by a factor of 1.4 to 2.6 and show no dependence on dwell time. Gardner and Denis [2004], Baker et al. [2006] and Gardner [2007b] also described experiments where BND values vary by factors of 1.2-10.7 but where BND values show no *t*-dependence. The independence of BND values from *T* and dwell time suggests that processes that would normally increase BND (e.g., multiple episodes of nucleation) are absent. Here, bubble nucleation appears to have occurred as a single event in all experiments.

In these experiments, bubbles grow progressively until the melt reaches the *T*-dependent $H_2O$ solubility limit at 0.1 MPa. As our experimental cores approach equilibrium, BSDs converge to a common distribution, irrespective of the experimental temperature (900-1100°C), dwell time (0.25-24 h), initial degree of $H_2O$ oversaturation (5-15%), or melt viscosity ($10^{5.7}$-$10^{8.1}$ Pa s) (Fig. 4; Table 3). In fact, the BSDs for samples that reach their equilibrium plateaus are virtually identical (Fig. 4). Tormaru [1989, 1995] has previously suggested that bubbles growing freely in a melt are expected to reach a size at equilibrium that is limited solely by surface tension ($\sigma$). Given that $\sigma$ is only weakly *T*-dependent [e.g., *Gardner and Ketcham,* 2011], we find Toramaru's [1989, 1995] statement to be consistent with our experimental results as we observe virtually the same mean bubble size in samples produced over a *T* span of >200°C.

## 6. A predictive model for magmatic vesiculation

Below we explore the relationships between calculated values of chemical affinity (*A* (kJ./mol)), melt viscosity (η (Pa s)), the observed final porosity (ϕ (%)), and average relative volume change rate (*dV/dt* ($h^{-1}$)) of the system. Chemical affinity constitutes the thermodynamic driving force for a chemical reaction and accounts for *T*, *P* and the $H_2O$ content of the melt. It can be calculated using estimates for the enthalpy and entropy of $H_2O$ exsolution (see below), the fugacity of $H_2O$ in the vapour, and calculated values for the activity of $H_2O$ in the melt (e.g., rhyolite-MELTS; *Gualda et al.*, 2012). Viscosity is the primary kinetic moderator in most polymerized melts and especially in melts having low $H_2O$ contents or near *Tg* [*Bagdassarov et al.*, 1996]. We use the correlations in these properties to guide our development of a time-dependent model that predicts the porosity of a silicic melt over a range of saturation states and temperatures.

## *6.1 Thermodynamic driving force*

The optimal values of ΔH° and ΔS° we derived for exsolution of $H_2O$ from a silicate melt, based on the Redlich-Kwong equation of state for $H_2O$, are 18.49 kJ/mol and 108.0 J/K mol, respectively (Fig. 5a; cf. *Ryan et al.*, 2015). These values are fully consistent with previous estimates of Zhang [1999], Yamashita [1999], and Liu et al. [2005]. We use these values to model the chemical affinity (*A*) for $H_2O$ exsolution in each experiment as a function of *T,* and the initial and final water contents of the melts (Fig. 5b; Table 3). Values of *A* track the degree of $H_2O$ oversaturation (*A* ~1-4 kJ/mol) resulting from the retrograde solubility of $H_2O$ at 0.1 MPa (~1.6 kJ/mol per 100°C). Our highest *T* experiment has the largest *A* for $H_2O$ exsolution (*A* ~4 kJ/mol).

## *6.2 Viscosity-controlled bubble growth rates*

Isobaric growth of a bubble in these experiments can be controlled by two kinetic processes: 1) the expansion of an over-pressurized bubble against the viscous melt, and 2) the diffusion of dissolved $H_2O$ into the bubble [*Sparks,* 1978; *Toramaru,* 1995; *Blower et al.,* 2001]. Expansion continues until a plateau is reached (e.g., Figs. 2,4,7) indicating the system has reached thermodynamic equilibrium. To establish that the system is at equilibrium and fully relaxed we have compared the characteristic timescales for diffusion ($\tau_D$) and viscous relaxation ($\tau_\eta$) to the experimental timescale ($\tau$) necessary to achieve equilibrium (Table 3). We have defined $\tau_D$ as $x^2/16D$ where $x$ is the average distance between bubbles in the plateau samples and $D$ is the diffusion rate of $H_2O$. Values of $\tau_\eta$ are approximated by $\eta/G$, where $\eta$ is the melt viscosity and G is the bulk shear modulus (~ $10^{10\pm0.5}$ Pa [*Dingwell and Webb,* 1990]).

We use the Deborah number (De), taken as $\tau_\eta/\tau$, to compare the viscous relaxation and experimental timescales (Table 3). Values of De for plateau samples are <<1 (i.e. $10^{-8}$-$10^{-7}$; Table 3), indicating that the melts in these experiments are fully relaxed. In a parallel fashion, the ratios of the diffusive to experimental timescales ($\tau_D/\tau$) are < 1 (0.03-0.14; Table 3), suggesting that, at the experimental temperatures, there has been sufficient time to ensure bubble growth is not diffusion limited (Table 3). Plateau samples are taken as representing fully relaxed, end states in the vesiculation process.

The average rates of volume (relative) change (*dV/dt*), calculated for each sample from the volume change relative to the initial volume, divided by the time taken to reach the plateau, are given in Table 3. An Arrhenius plot of *dV/dt vs*. reciprocal $T$ (Fig. 6b) suggests an activation energy ($E_{dV/dt}$) of 269 kJ/mol (Supporting Information Text S3). The corresponding activation energy for viscous flow ($E_\eta$) of these melts [*Giordano et al.,* 2008] is ~369 kJ/mol (Supporting Information Text S3). The calculated activation energy for $H_2O$ diffusion ($E_D$) in these melts [*Zhang et al.,* 2007] is 77 kJ/mol (Supporting Information Text S3). Comparison of the observed activation energy for vesiculation to the modeled activation energies for viscous flow and diffusion suggests viscous flow processes dominate *dV/dt* and vesiculation. Bagdassarov et al.'s [1996] experimental study of weakly $H_2O$-oversaturated rhyolitic melts also concluded that, near *Tg*, vesiculation was controlled by the viscous relaxation of the melt (Supporting Information Text S3).

Values of *dV/dt* show a strong inverse correlation with melt viscosity (Fig. 6b). Whilst *A* controls the total potential for $H_2O$ exsolution, η moderates the rate of vesiculation and bubble growth [cf. *Sparks,* 1978; *Lyakhovsky et al.,* 1996; *Navon et al.,* 1998; *Proussevitch and Sahagian,* 1998; *Blower et al.,* 2001; *Masotta et al.,* 2014]. The linear scaling of these parameters in log-log space means that where viscosity spans several orders of magnitude (Table 3), average volume change rate will as well.

### *6.3 A predictive model*

We use these experimental results to construct a model for predicting the rate of vesiculation and the final porosity for oversaturated silicate melts. The model has a functional form similar to the Avrami equation [*Avrami,* 1940], a generic equation that is used to model kinetically controlled thermochemical processes (e.g., polymer crystallization [*Lorenzo et al.,* 2007], crystal growth in glasses [*Málek,* 1995], bubble growth in melts [*Bagdassarov et al.,* 1996]). The simplest form of the equation is:

$$\Delta V(t) \sim 1 - \exp[-(k\mathrm{t})^n] \qquad (1)$$

where *k* and *n* are kinetic constants [*Málek,* 1995]. Here we assume an Avrami exponent (i.e., *n*) of 1. Based on our observation that the rate of volume change correlates strongly with melt viscosity (η), we have replaced the term *kt* with $\gamma t/\eta$ where $\gamma$ is an unknown adjustable coefficient. This substitution explicitly links the kinetic moderator (i.e., *k*) to the rate at which volume increases and porosity develops (i.e., exsolution and expansion of the fluid phase). In addition to the rate of volume expansion, our model needs to accurately predict the extent of vesiculation, which reflects the degree of $H_2O$ supersaturation. We have, therefore, introduced a pre-exponential term for the thermodynamic potential for vesiculation (i.e. affinity, $A$). In order to capture the entire experimental dataset we included two adjustable parameters ($\alpha$ and $\beta$):

$$\phi = \alpha A^{\beta} \left(1 - \exp \frac{-\gamma t}{\eta}\right) \qquad (2)$$

The observed variables derived from the experiments include porosity ($\phi$; %) and time ($t$; s). Independent calculated variables include estimates of the affinity for $H_2O$ exsolution ($A$; J/mol) and the viscosity ($\eta$; Pa s) of the melt.

The adjustable parameters $\alpha$, $\beta$, and $\gamma$ have optimal values of 25.8, 0.1143, and 2109, respectively (Figs. 7). The term $\alpha A^{\beta}$ controls the final plateau value of the curve, whereas, the rate of vesiculation (i.e. slope of the curve) is controlled by the term $\gamma t/\eta$. The covariance ellipse for $\alpha$ and $\gamma$ values, computed for the optimal value of $\beta$ (i.e. 0.1143), shows the parameters to be well constrained and moderately independent and not excessively correlated (Fig. 7c).

Model lines for each temperature suite are compared to the original data in Figure 7a. The model successfully recovers final plateau porosity values for all temperature suites. Figure 7b shows observed and modelled values for $\phi$. The greatest differences between model and data are found at low values of porosity (<20 %) and especially in the high temperature experiments at small times. In these particular experiments, our model predicts the extent of vesiculation well, but predicts a quicker onset to vesiculation and a lower average rate of vesiculation (less steep curve). The discrepancies between the model and samples from the lowest temperature dataset (i.e., 900°C) reflect the increased experimental uncertainty associated with producing these samples (Fig. 7a,b).

## 7. Discussion

### *7.1 Model Verification*

Our time-dependent model for vesiculation is calibrated on vesiculation experiments performed on weakly $H_2O$-oversaturated silicic melts at 0.1 MPa. It is most relevant as a forensic or predictive tool when applied to low-pressure volcanic environments involving weakly $H_2O$-oversaturated melts. However, by incorporating the variables affinity ($A$) and melt viscosity ($\eta$), the model has the potential to be extended and applied to vesiculation in other volcanic systems (e.g., domes, spines, effusive lavas).

We demonstrate this by applying the model to the experimental dataset of Bagdassarov et al. [1996]. In their study the authors heated natural, weakly $H_2O$-oversatured (~0.14 wt% $H_2O$), peralkaline rhyolite to a set temperature (630-925°C) above $Tg$ (530°C) in order to induce vesiculation at atmospheric pressure. The change in the volume of the sample ($V_{gas}/V_{melt}$) that resulted from bubble nucleation and growth was monitored by dilatometry [*Bagdassarov et al.,* 1996]. The similarity of the starting material, both in terms of composition and saturation state, as well as the experimental methodology, makes this study an excellent test of the model developed here.

The Bagdassarov et al. [1996] dataset comprises measurements of (increasing) relative sample volume with time as the samples vesiculate and expand, and is reported only graphically. We have extracted several data points from their Figure 7 ($t$ (s) vs. $V_{gas}/V_{melt}$) that represent the porosity development in the 805°C and 883°C experiments, and plotted them in Figure 8a with a conservative uncertainty of 5%. We have then used their reported melt composition and $H_2O$ content to compute melt viscosity using the model of Giordano et al. [2008] and the affinity for vesiculation [*Ryan et al.,* 2015]. The model represented by Eq. 2, combined with these input variables, generate model curves that have very similar forms to the trends defined by the original data (Fig. 8a). More importantly, the model curves capture the absolute values of the original data, including the final values of $\phi$ and the time necessary to achieve the peak $\phi$, to within experimental uncertainty.

The remainder of the Bagdassarov et al. [1996] data are summarized only in a plot of log (*t*) vs. log ($V_{gas}/V_{melt}$). These experiments spanned a temperature range of 665-916°C. We have used Eq. 2 to make predictive curves for these datasets and plotted the resulting model curves in Fig. 8. For comparison, the inset to this figure shows Bagdassarov et al.'s [1996] original data as trend lines produced by tracing points in the original figure. Our model predicts the reported extent and rates of vesiculation well, despite the presence of other volatile species (F, Cl) in their starting material that are not accounted for in our model.

Stevenson et al. [1997] offer a similar suite of experiments involving atmospheric heating of natural $H_2O$-rich (~1.8 wt% $H_2O$) rhyolite to $T>Tg$ for prescribed temperatures and monitoring sample volume with dilatometry [cf. *Bagdassarov et al.,* 1996]. In this case, our model predicted curves that exactly paralleled the expansion curves published by Stevenson et al. [1997] but were displaced to substantially longer times. Interestingly, if the melt viscosity was assumed to be 2 orders of magnitude lower than reported for each experiment, our model provides a very good approximation to the entire original dataset. The failure of our model to reproduce this dataset may well reflect the nature of the natural obsidian used in their experiments. As described by Stevenson et al. [1997], the obsidian contained ≤ 1% microlites of plagioclase and biotite, ~6 vol. % water filled vesicles, and minor flow banding where vesicle content was ~9 vol.%. If vesiculation were to be at least partially accommodated by growth of pre-existing bubbles, or if nucleation was facilitated by the presence of microlites, the observed rates of volume increase would be higher than expected for the reported melt viscosity. We suggest that the initial properties of the experimental cores may have accelerated the vesiculation and gas expansion processes during their isothermal experiments, causing our model to overshoot the observed data in time.

## *7.2 Regime diagrams*

We have explored the capacity of the model to be extrapolated and used on natural systems by defining two dimensionless parameters. Specifically, we define dimensionless time ($t_D$) as $t/\tau_\eta$, where $\tau_\eta$ is the viscous relaxation timescale given by $\eta$/G (see above). Dimensionless vesiculation rate ($R_D$) is defined as $\phi'/\phi'_{max}$, where $\phi'$ is the modelled vesiculation rate at a specific time and $\phi'_{max}$ is the maximum modelled vesiculation rate occurring at $t$~0. Both have the units of percent change per second.

In our model the extent of vesiculation is dictated by the degree of $H_2O$-oversaturation, which is itself expressed as chemical affinity ($A$). Substituting the dimensionless time parameter ($t_D$) into Eq. 2 allows the effects of $A$ on the transient porosity of the rhyolite magma to be isolated. This substitution replaces $t/\eta$ with $t_D$/G:

$$\phi = \alpha A^{\beta} \left(1 - \exp\frac{-\gamma t_D}{G}\right) \qquad (3)$$

thereby facilitating computation of universal porosity production curves. The model curves in Figure 9a illustrate the effects of $A$ on the total amount of vesiculation for any melt viscosity. As dimensionless time increases, porosity increases steeply to a final value that defines a horizontal plateau dictated by the magnitude of $A$. At $A$=0 there is no vesiculation.

With increasing $A$ the initial slopes of the model curves increase (Fig. 9a). The change in slope is a consequence of the $A$-dependence of the vesiculation rate ($\phi'$), derived from Eq. 2:

$$\phi' = \frac{d\phi}{dt} = \frac{\alpha\,\gamma}{\eta} A^{\beta} \left(\exp\frac{-\gamma t}{\eta}\right) \qquad (4)$$

This expression highlights that while η exerts a primary control on vesiculation rate, there is also a significant contribution from *A*. At constant *A*, the vesiculation rate has a maximum ($\phi'_{max}$) at *t* ~0:

$$\phi'_{\mathrm{Max}} = \frac{\alpha\gamma}{\eta} A^{\beta} \qquad (5)$$

which we use to define a dimensionless vesiculation rate parameter ($R_D = \phi'/\phi'_{max}$). Expressed in terms of dimensionless time ($t_D$) we obtain:

$$R_D = \mathrm{e}^{\frac{-\gamma\, t_D}{G}} \qquad (6)$$

Figure 9b shows the universal curve generated by Eq. 6 that tracks the decay in vesiculation rate relative to dimensionless time. The absolute rates and extent of vesiculation vary as a function of melt properties but in terms of dimensionless time, where time is scaled to melt relaxation timescales, rates of exsolution decay systematically along the universal curve. Vesiculation rate decays rapidly to reach 50% of the maximum rate at $t_D \sim 10^{6.4}$; vesiculation ceases at $t_D > 10^{7.5}$ (Fig. 9b). Superimposed on the same diagrams (Fig. 9a,b) are characteristic times for a melt having a viscosity of $10^8$ Pa s.

### *7.3 Model consequences*

Our model is most relevant to experimental or natural systems that are only weakly $H_2O$ oversaturated; it is likely to have less applicability to volcanic systems operating far from chemical equilibrium (e.g., explosive systems). To demonstrate the model's potential use we have simulated the isothermal ascent and concomitant vesiculation of hydrous rhyolite magma as a function of magma ascent rate (Fig. 10).

The model calculations use a rhyolitic melt composition and pre-eruption temperature (860 °C) from the Rattlesnake Tuff as reported by Streck and Grunder [1995], assuming an initial $H_2O$ content of 2.0 wt.%. Given these initial conditions we use the program rhyolite-

MELTS [*Gualda et al.*, 2012] to simulate the thermodynamic state of the magma as it ascends isothermally and undergoes equilibrium vesiculation. The result of this simulation is a set of points on the equilibrium degassing path that define 1) the depth of volatile saturation for the melt (~1450 m), 2) the decrease in the melt's water content, and 3) the increase in the vol.% of the gas phase as a function of pressure (i.e., depth; Fig. 10a). The viscosity of the melt phase along this path increases due to the loss of dissolved $H_2O$ (Fig. 10b) and is calculated using the GRD model [*Giordano et al.*, 2008].

In contrast to the equilibrium vesiculation paths shown in Figure 10, we have used Eq. 2 to model the extent of vesiculation (i.e., porosity) in the ascending magma for a range of magma rise rates. We use rhyolite-MELTS to predict values of affinity for $H_2O$ exsolution in the rising (isothermal) melt as a function of pressure and $H_2O$ content. Operationally, the volume of exsolved volatile predicted by rhyolite-MELTS is taken as equal to $\alpha A^{\beta}$ at times corresponding to $t_D > 10^{7.5}$ s (Fig. 9) when equilibrium, and peak vesiculation, are reached:

$$\alpha A^{\beta} = \phi_{melts}\left(1 - \exp\frac{-\gamma 10^{7.5}}{G}\right)^{-1} \sim \phi_{melts} \qquad (7)$$

Fluid saturation occurs at ~ 1450 m depth after which vesiculation begins; the extent of vesiculation during ascent represents the competition between the predicted time dependent vesiculation (Eq. 2) and the magma rise rate. At low ascent rates ($< 0.001$ m s$^{-1}$) the extent of vesiculation predicted by our model (Eq. 2) is equal to the equilibrium exsolution path (Fig. 10a; heavy line). As ascent rate increases the departure from the equilibrium end-member increases. At rise rates in excess of 0.5 m s$^{-1}$, vesiculation is greatly inhibited and the magma reaches the eruption point in a highly oversaturated state. Such systems have substantial amounts of stored energy for driving explosive eruption.

We have plotted two shaded fields for estimations of magma rise rates attending slow extrusion of rhyolite lava and domes (D) ($10^{-5}$ to $10^{-2}$ m/s; cf. *Takeuchi et al.*, 2009) and the range of "fast" rise rates estimated for the 2008 explosive-to-effusive Chaitén eruption (Ch) (0.05 - 0.5 m/s; *Castro and Dingwell,* 2009). Magmas that rise at rates typical for dome growth remain at or near equilibrium conditions, and reach the surface with high porosities and low degrees of supersaturation, favouring quiescent extrusion. In contrast, at the rates inferred for the Chaitén eruption the time necessary for extensive vesiculation exceeds the ascent time, resulting in significant oversaturation. At these conditions the energy stored in the magma may be dissipated be explosive behaviour, and hybrid or explosive-to-effusive eruption dynamics can commence.

Finally, we have explored the rheological consequences of vesiculation in the rising rhyolite magma where increasing porosity has the potential to reduce the bulk viscosity of the bubbly magma [cf. *Llewellin and Manga* 2005; *Mader et al.* 2013]. We have used the phenomenological model advanced by Quane and Russell [2005] and refined by Quane et al. [2009]. Their model uses an empirical equation developed by Rahaman et al. [1987] and Ducamp and Raj [1989] to predict the bulk viscosity of a porous material ($\eta_{b;}$ Pa s) as a function of porosity ($\phi$; %) and melt viscosity ($\eta_{m;}$ Pa s):

$$log\,\eta_b = log\,\eta_m - K\,\frac{\phi}{100-\phi} \qquad (8)$$

where *K* (*K*=0.78 [*Quane et al.* 2009]) is an experimentally derived exponential constant [cf. *Mader et al.*, 2013; *Heap et al.*, 2014]. Values of $\eta_m$ are adjusted and increase as the melt exsolves $H_2O$ during ascent; the curves for the magma viscosity presented in Fig. 10b reflect the relative and competing effects of increasing melt viscosity due to $H_2O$ loss (Fig. 10b; heavy line on left) and decreasing bulk viscosity due to increasing porosity. Depending on the ascent rate, magma viscosity can increase or decrease; slow ascent (i.e., lavas & domes) allows for maximum vesiculation and maximum (> 2 orders of magnitude) decrease in bulk magma viscosity. This is contrast to a model path that might assume equilibrium vesiculation and complete degassing (i.e. no porosity) during ascent; such a path would cause an increase in *magma* (i.e. melt) viscosity of > 2 orders of magnitude.

## 8. Summary

As magmas ascend to the surface, bubbles form as a consequence of the evolving saturation state of volatiles dissolved in the melt. The extent of oversaturation is dictated by the thermodynamic state of the magma (chemical affinity). The response to oversaturation is kinetically moderated by diffusive timescales at high temperatures and the viscous timescales as temperatures approach the *Tg* of the melt [e.g., *Bagdassarov et al.*, 1996]. In this regard, the kinetic and thermodynamic properties governing vesiculation processes are critical elements in explaining the observed variations in effusive styles of volcanism.

In this experimental study, we have used XCT data from foamed rhyolitic obsidian cores to describe bubble nucleation and growth dynamics over a range of temperatures (900-1100°C), dwell times (0.25-24 h) and initial states of oversaturation (5-15% greater than $H_2O$ solubility limits) at atmospheric pressure. The experiments return: i) the time-dependent porosity evolution within melts at different temperatures, ii) the change in BSDs with time approaching thermodynamic equilibrium, and iii) evidence of common nucleation and growth mechanisms within our system. Additionally, the present study demonstrates the power of XCT methods for placing kinetic experiments of magmatic systems on a powerfully statistical basis, which can serve as a robust test bed for evaluating competing reaction mechanisms for the kinetics of phase separation processes in volcanic systems.

We used these experimental data to calibrate an empirical time-dependent model for rates and extent of vesiculation of silicate melts. Our model has the following attributes: i) it reproduces our data to within experimental uncertainty, ii) it reproduces other published experimental datasets [e.g., *Bagdassarov et al.,* 1996], iii) the model incorporates a fundamental and predictable [e.g., *Giordano et al.,* 2008] transport property (e.g., $\eta$) that is relevant to all silicate melts on Earth and other planetary bodies, and iv) it has a thermodynamic basis ($A$) that is a function of pressure, temperature and $H_2O$ content. The latter point allows extension to other natural systems at near-equilibrium conditions, despite the model being calibrated on low-pressure rhyolitic melts. For example, the model should find applications in forecasting the rates and extents of vesiculation in lavas, post-depositional ignimbrites, or within volcanic conduits.

## Acknowledgements

The authors are indebted to Hugh Tuffen (Lancaster University, UK) who generously donated the block of obsidian from Hrafntinnuhryggur, Krafla, Iceland used in this study. AGR acknowledges scholarship and travel funding from AmeriCorps, the Mineralogical Association of Canada and the University of British Columbia. The NSERC Discovery and Discovery Accelerator Supplements programs and the German Academic Exchange Service funded this work via grants held by JKR. DBD acknowledges the support of ERC Advanced Investigator Grant no. 247076 “EVOKES” (Explosive Volcanism in the Earth System). ABP acknowledges funding from the Canadian Foundation for Innovation.

## References

Avrami, M (1940) Kinetics of Phase Change. II Transformation-Time Relations for Random Distributions of Nuclei. Journal of Chemical Physics, 8, 212–224.

Bagdassarov, N.S., and Dingwell, D.B. (1992) A rheological investigation of vesicular rhyolite. Journal of Volcanology and Geothermal Research, 50, 307-322.

Bagdassarov, N.S., Dingwell, D.B., and Wilding, M.C. (1996) Rhyolite magma degassing: an experimental study of melt vesiculation. Bulletin of Volcanology, 57, 587–601.

Bai, L., Baker, D.R., and Rivers, M. (2008) Experimental study of bubble growth in Stromboli basalt melts at 1 atm. Earth and Planetary Science Letters, 267, 533–547.

Baker, D.R., Lang, P., Robert, G., Bergevin, J.-F., Allard, E., and Bai, L. (2006) Bubble growth in slightly supersaturated albite melt at constant pressure. Geochimica et Cosmochimica Acta, 70, 1821–1838.

Baker, D.R., Brun, F., O'Shaughnessy, C., Mancini, L., Fife, J.L., and Rivers, M. (2012) A four-dimensional X-ray tomographic microscopy study of bubble growth in basaltic foam. Nature Communications, 3, 1135.

Blower, J.D., Mader, H.M., and Wilson, S.D.R. (2001) Coupling of viscous and diffusive controls on bubble growth during explosive volcanic eruptions. Earth and Planetary Science Letters, 193, 47–56.

Blower, J.D., Keating, J.P., Mader, H.M., and Phillips, J.C. (2002) The evolution of bubble size distributions in volcanic eruptions. Journal of Volcanology and Geothermal Research, 120, 1–23.

Burgisser, A., and Gardner, J.E. (2005) Experimental constraints on degassing and permeability in volcanic conduit flow. Bulletin of Volcanology, 67, 42–56.

Cas, R.A.F., and Wright, J.V. (1987) Volcanic Successions: Modern and Ancient, 528 p. Chapman and Hall, London.

Castro, J.M., and Dingwell, D.B. (2009) Rapid ascent of rhyolitic magma at Chaitén volcano, Chile. Nature, 461, 780-784.

Castro, J.M., Manga, M., and Martin, M.C. (2005) Vesiculation rates of obsidian domes inferred from $H_2O$ concentration profiles. Geophysical Research Letters, 32, L21307.

Castro, J.M., Beck, P., Tuffen, H., Nichols, A.R.L., Dingwell, D.B., and Martin, M.C. (2008) Timescales of spherulite crystallization in obsidian inferred from water concentration profiles. American Mineralogist, 93, 1816–1822.

Castro, J.M., Burgisser, A., Schipper, C.I., and Mancini, S. (2012) Mechanisms of bubble coalescence in silicic magmas. Bulletin of Volcanology, 74, 2339-2352.

Crank, J. (1975) The Mathematics of Diffusion, 414 p. Claredon Press, Oxford.

Deans, S.R. (2007) The radon transform and some of its applications, 295 p. Dover Publishing Company, New York.

Dingwell, D.B., and Webb, S.L. (1990) Relaxation in silicate melts. European Journal of Mineralogy, 2, 427–449.

Ducamp, V.C., and Raj, R. (1989) Shear and densification of glass powder compacts. Journal of the American Ceramic Society, 72, 798-804.

Fife, J.L., Rappaz, M., Pistone, M., Celcer, T., Mikuljan, G., and Stampanoni, M. (2012) Development of a laser-based heating system for in situ synchrotron-based X-ray tomographic microscopy. Journal of Synchrotron Radiation, 19, 352-358.

Gaonac'h, H., Lovejoy, S., Stix, J., and Scherzter, D. (1996) A scaling growth model for bubbles in basaltic lava flows. Earth and Planetary Science Letters, 139, 395–409.

Gardner, J.E. (2007a) Bubble coalescence in rhyolitic melts during decompression from high pressure. Journal of Volcanology and Geothermal Research, 166, 161-176.

Gardner, J.E. (2007b) Heterogeneous bubble nucleation in highly viscous silicate melts during instantaneous decompression from high pressure. Chemical Geology, 236, 1-12.

Gardner, J.E., and Denis, M.-H. (2004) Heterogeneous bubble nucleation on Fe-Ti oxide crystals in high-silica rhyolitic melts. Geochimica et Cosmochimica Acta, 68, 3587-3597.

Gardner, J.E., and Ketcham, R.A. (2011) Bubble nucleation in rhyolite and dacite melts: temperature dependence of surface tension. Contributions to Mineralogy and Petrology, 162, 929–943.

Gardner, J.E., Hilton, M., and Carroll, M.R. (1999) Experimental constraints on degassing of magma: isothermal bubble growth in continuous decompression from high pressure. Earth and Planetary Science Letters, 168, 201-218.

Gardner, J.E., Hilton, M., and Carroll, M.R. (2000) Bubble growth in highly viscous silicate melts during continuous decompression from high pressure. Geochimica et Cosmochimica Acta, 64, 1473–1483.

Giachetti, T., Bruitt, T.H., Burgisser, A., Arbaret, L., and Galven, C. (2010) Bubble nucleation, growth and coalescence during the 1997 Vulcanian explosions of Soufrière Hills Volcano, Montserrat. Journal of Volcanology and Geothermal Research, 193, 215–231.

Giordano, D., Russell, J.K., and Dingwell, D.B. (2008) Viscosity of magmatic liquids: A model. Earth and Planetary Science Letters, 271, 123–134.

Gonde, C., Martel, C., Pichavant, M., and Bureau, H. (2011) In situ bubble vesiculation in silicic magmas. American Mineralogist, 96, 111–124.

Gonnermann, H.M., and Gardner, J.E. (2013) Homogeneous bubble nucleation in rhyolitic melt: Experiments and nonclassical theory. Geochemistry Geophysics Geosystems, 14, 4758–4773.

Gualda, G.A.R., Ghiorso, M.S., Lemons, R.V., and Carley, T.L. (2012) Rhyolite-MELTS: A modified calibration of MELTS optimized for silica-rich, fluid-bearing magmatic systems. Journal of Petrology, 53, 875-890.

Hamada, M., Laporte, D., Cluzel, N., Koga, K.T., and Kawamoto, T. (2010) Simulating bubble number density of rhyolitic pumices from Plinian eruptions: constraints from fast decompression experiments. Bulletin of Volcanology, 72, 735-746.

Heap, M.J., Kolzenburg, S., Russell, J.K., Campbell, M.E., Welles, J., Farquharson, I.J., and Ryan, A. (2014), Conditions and timescales for welding block-and-ash flow deposits. Journal of Volcanology and Geothermal Research, 289, 202-209.

Hess, K.-U., and Dingwell, D.B. (1996) Viscosities of hydrous leucogranitic melts: A non-Arrhenian model. American Mineralogist, 81, 1297-1300.

Huber, C., Su, Y., Nguyen, C.T., Parmigiani, A., Gonnermann, H.M., and Dufek, J., (2014) A new bubble dynamics model to study bubble growth, deformation and coalescence. Journal of Geophysical Research, 119, 216-239.

Hurwitz, S., and Navon, O. (1994) Bubble nucleation in rhyolitic melts: Experiments at high pressure, temperature and water content. Earth and Planetary Science Letters, 122, 267–280.

L'Heureux, I. (2007) A new model of volatile bubble growth in a magmatic system: Isobaric case. Journal of Geophysical Research, 112, B12208.

Larsen, J.F., and Gardner, J.E. (2000) Experimental constraints on bubble interactions in rhyolite melts: implications for vesicle size distributions. Earth and Planetary Science Letters, 180, 201–214.

Larsen, J.F., Denis, M.-H., and Gardner, J.E. (2004) Experimental study of bubble coalescence in rhyolitic and phonolitic melts. Geochimica et Cosmochimica Acta, 68, 333-344.

Lensky, N.G., Navon, O., and Lyakhovsky, V. (2004) Bubble growth during decompression of magma: experimental and theoretical investigation. Journal of Volcanology and Geothermal Research, 129, 7–22.

Liu, Y., and Zhang, Y. (2000) Bubble growth in rhyolitic melt. Earth and Planetary Science Letters, 181, 251-264.

Liu, Y., Zhang, Y., and Behrens, H. (2005) Solubility of $H_2O$ in rhyolitic melts at low pressures and a new empirical model for mixed $H_2O$-$CO_2$ solubility in rhyolitic melts. Journal of Volcanology and Geothermal Research, 143, 219–235.

Llewellin, E.W., and Manga, M. (2005) Bubble suspension rheology and implications for conduit flow. Journal of Volcanology and Geothermal Research, 143, 205-217.

Lorenzo, A.T., Arnal, M.L., Albuerne, J., and Müller, A.J. (2007) DSC isothermal polymer crystallization kinetics measurements and the use of the Avrami equation to fit the data: Guidelines to avoid common problems. Polymer Testing, 26, 222-231.

Lyakhovsky, V., Hurwitz, S., and Navon, O. (1996) Bubble growth in rhyolitic melts: experimental and numerical investigation. Bulletin of Volcanology, 58, 19–32.

Mader, H.M., Llewellin, E.W., and Mueller, S.P. (2013) The rheology of two-phase magmas: A review and analysis. Journal of Volcanology and Geothermal Research, 257, 135-158.

Málek, J. (1995) The applicability of Johnson-Mehl-Avrami model in the thermal analysis of the crystallization kinetics of glasses. Thermochimica Acta. 267, 61-73.

Mangan, M.T., and Cashman, K.V. (1996) The structure of basaltic scoria and reticulite and inferences for vesiculation, foam formation, and fragmentation in lava fountains. Journal of Volcanology and Geothermal Research, 73, 1–18.

Mangan, M., and Sisson, T. (2000) Delayed, disequilibrium degassing in rhyolite magma: decompression experiments and implications for explosive volcanism. Earth and Planetary Science Letters, 183, 441-455.

Martel, C., and Bureau, H. (2001) In situ high-pressure and high-temperature bubble growth in silicic melts. Earth and Planetary Science Letters, 191, 115-127.

Martel, C., and Iacono-Marziano, G. (2015) Timescales of bubble coalescence, outgassing, and foam collapse in decompressed rhyolitic melts. Earth and Planetary Science Letters, 412, 173-185.

Marxer, H., Bellucci, P., and Nowak, M. (2015) Degassing of $H_2O$ in a phonolitic melt: A closer look at decompression experiments. Journal of Volcanology and Geothermal Research, 297, 109-124.

Masotta, M., Ni, H., and Keppler, H. (2014) In situ observations of bubble growth in basaltic, andesitic and rhyodacitic melts. Contributions to Mineralogy and Petrology, 167, 976.

McIntosh, I.M., Llewellin, E.W., Humphreys, M.C.S., Nichols, A.R.L., Burgisser, A., Schipper, C.I., and Larsen, J.F. (2014) Distribution of dissolved water in magmatic growth records growth and resorption of bubbles. Earth and Planetary Science Letters, 401, 1-11.

Mourtada-Bonnefoi, C.C., and Laporte, D. (2004) Kinetics of bubble nucleation in a rhyolitic melt: an experimental study of the effect of ascent rate. Earth and Planetary Science Letters, 218, 521–537.

Navon, O., Chekhmir, A., and Lyakhovsky, V. (1998) Bubble growth in highly viscous melts: theory, experiments, and autoexplosivity of dome lavas. Earth and Planetary Science Letters, 160, 763–776.

Nowak, M., Cichy, S.B., Botcharnikov, R.E., Walker, N., and Hurkuck, W. (2011) A new type of high-pressure low-flow metering valve for continuous decompression: First experimental results on degassing of rhyodacitic melts. American Mineralogist, 96, 1373-1380.

Phillion, A.B., Lee, P.D., Maire, E., and Cockcroft, S.L. (2008) Quantitative Assessment of Deformation-Induced Damage in a Semisolid Aluminum Alloy via X-ray Microtomography. Metallurgical and Materials Transactions A, 39A, 2459–2469.

Pistone, M., Caricchi, L., Ulmer, P., Reusser, E., and Ardia, P. (2013) Rheology of volatile-bearing crystal mushes: Mobilization vs. viscous death. Chemical Geology, 345, 16-39.

Proussevitch, A.A., and Sahagian, D.L. (1998) Dynamics and energetics of bubble growth in magmas: Analytical formulation and numerical modeling. Journal of Geophysical Research, 103, B8, 18223–18251.

Proussevitch, A.A., Sahagian, D.L., and Tsentalovich, E.P. (2007) Statistical analysis of bubble and crystal size distributions: Formulations and procedures. Journal of Volcanology and Geothermal Research, 164, 95-111.

Quane, S.L., and Russell, J.K. (2005) Welding: insights form high-temperature analogue experiments. Journal of Volcanology and Geothermal Research, 142, 67-87.

Quane, S.L., Russell, J.K. and Friedlander, E.A. (2009) Time scales of compaction in volcanic systems. Geology, 37, 471-474.

Rahaman, M.N., de Jonghe, L.C., Scherer, G.W., and Brook, R.J. (1987) Creep and densification during sintering of glass powder compacts. Journal of the American Ceramic Society, 70, 766-774.

Ryan, A.G., Russell, J.K., Nichols, A.R.L., Hess, K.-U., and Porritt, L.A., (2015) Experiments and models on $H_2O$ retrograde solubility in volcanic systems. American Mineralogist, 100, 774-786.

Schneider, C.A., Rasband, W.S., and Eliceiri, K.W. (2012) NIH Image to ImageJ: 25 years of image analysis. Nature Methods, 9, 671–675.

Shea, T., Houghton, B.F., Gurioli, L., Cashman, K.V., Hammer, J.E., and Hobden, B.L. (2010) Textural studies of vesicles in volcanic rocks: An integrated methodology. Journal of Volcanology and Geothermal Research, 190, 271–289.

Sparks, R.S.J. (1978) The dynamics of bubble formation and growth in magmas: A review and analysis. Journal of Volcanology and Geothermal Research, 3, 1–37.

Stevenson, R.J., Bagdassarov, N.S., and Romano, C. (1997) Vesiculation processes in a water-rich calc-alkaline obsidian. Earth and Planetary Science Letters, 146, 555–571.

Streck, M.J., and Grunder, A.L. (1995) Crystallization and welding variations in a widespread ignimbrite sheet; the Rattlesnake Tuff, eastern Oregon, USA. Bulletin of Volcanology, 57, 151-169.

Takeuchi, S., Tomiya, A., and Shinohara, H. (2009) Degassing conditions for permeable silicic magmas: Implications from decompression experiments with constant rates. Earth and Planetary Science Letters, 283, 101-110.

Toramaru, A. (1989) Vesiculation Process and Bubble Size Distributions in Ascending Magmas with Constant Velocities. Journal of Geophysical Research, 94, B12, 17523–17542.

Toramaru, A. (1995) Numerical study of nucleation and growth of bubbles in viscous magmas. Journal of Geophysical Research, 100, B2, 1913–1931.

Tuffen, H., and Castro, J.M. (2009) The emplacement of an obsidian dyke through thin ice: Hrafntinnuhryggur, Krafla Iceland. Journal of Volcanology and Geothermal Research, 185, 352–366.

von Aulock, F.W., Wadsworth, F.B., Kennedy, B.M., and Lavallee, Y. (2015) Self Sealing Magmas. General Assembly of the European Geosciences Union (EGU), Vienna, Austria, Geophysical Research Abstracts, Vol. 17, EGU2015-9295..

Vona, A., Romano, C., Giordano, D., and Russell, J.K. (2013) The multiphase rheology of magmas from Monte Nuovo (Campi Flegrei, Italy). Chemical Geology, 346, 213–227.

Watkins, J.M., Manga, M., and DePaolo, D.J. (2012) Bubble geobarometry: A record of pressure changes, degassing, and regassing at Mono Craters, California. Geology, 40, 699-702.

Yamashita, S. (1999) Experimental Study of the Effect of Temperature on Water Solubility in Natural Rhyolite Melt to 100 MPa. Journal of Petrology, 40, 1497–1507.

Zhang, Y. (1999) Exsolution enthalpy of water from silicate liquids. Journal of Volcanology and Geothermal Research, 88, 201–207.

Zhang, Y., Xu, Z., Zhu, M., and Wang, H. (2007) Silicate melt properties and volcanic eruptions. Reviews of Geophysics, 45, RG4004.

# Figure Captions

**Figure 1.** Photographs of the undeformed starting material and experimental run-products. Pre-experiment material is shown as (a) starting core geometry, (b) thin section, and (c) SEM photomicrograph (see text). Post-experimental foamed cores from the 1000°C suite of experiments are shown for various dwell times: (d) 0.5 h, (e) 4 h, and (f) 13 h showing volume increase due to vesiculation. Scale bar is marked in mm.

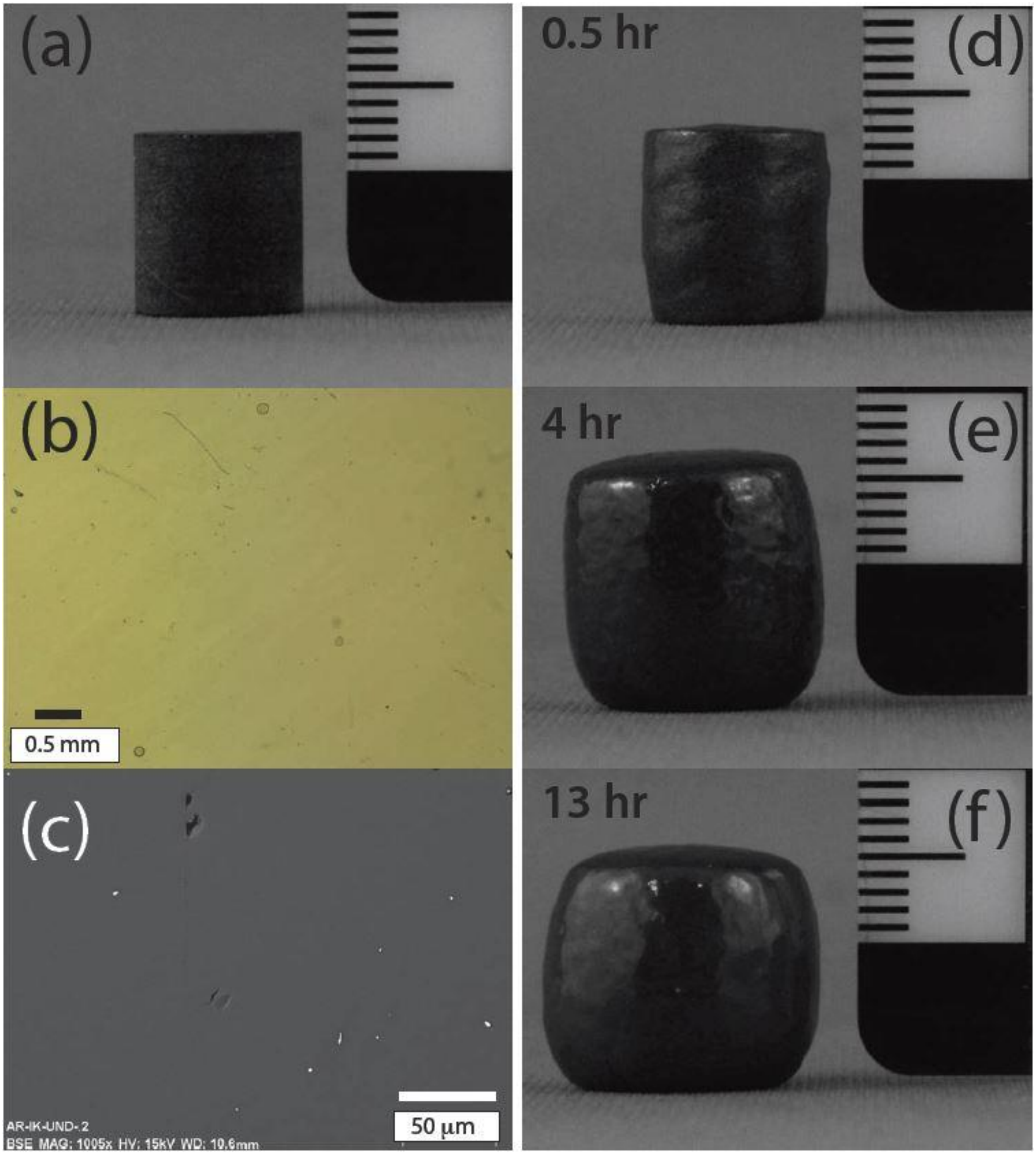

**Figure 2.** Measured porosity values for all experimental products. (a) Porosity ($\phi$) measured on 3D-XCT images using Avizo® Fire ($\phi_{AF}$) compared to He-pycnometry ($\phi_{HP}$) measurements. Closed symbols are replicate measurements for two samples having low and high porosity. (b) Experimental data plotted as porosity ($\phi$) *vs*. time ($t$) for all $T$-suites (900 - 1100°C). Trend lines show non-linear increases in $\phi$ with $t$ for each isothermal suite until reaching a plateau value. With increasing $T$ the rate of vesiculation (i.e. slope) and the final plateau value (maximum $\phi$) increase. The change in plateau value reflects the $T$-dependence of $H_2O$ solubility [*Ryan et al.*, 2015].

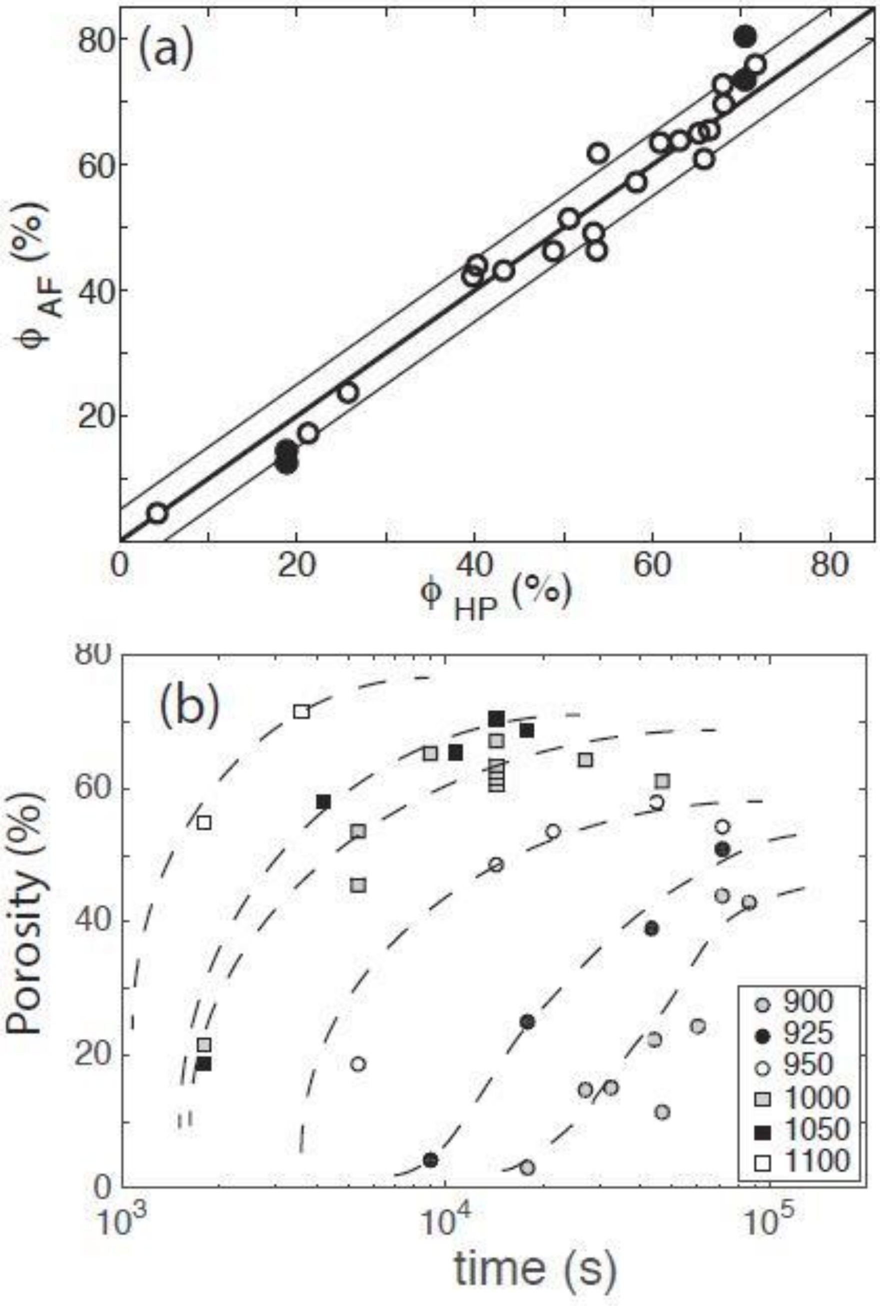

**Figure 3.** Bubble size distribution curves for experimental run products. Cumulative volume fraction ($\Sigma V$) of bubbles for a given radius (r) are plotted for samples having total porosity (ϕ) ranges of: (a) 0-25%, (b) 40-59%, and (c) 60-75%. BSD statistics are shown in the upper left corner: median bubble size ($r_{med}$), graphic standard deviation ($r_{\sigma}$), and skewness ($r_{\alpha}$). Cumulative number of bubbles ($\Sigma N$) having radii > r are plotted for isothermal suites (d) 925°C, (e) 1000°C, and (f) 1050°C. The dwell time (h) and porosity (%) of each sample are listed in lower left of each figure. Plateau samples (Fig. 2b) are denoted by solid black lines.

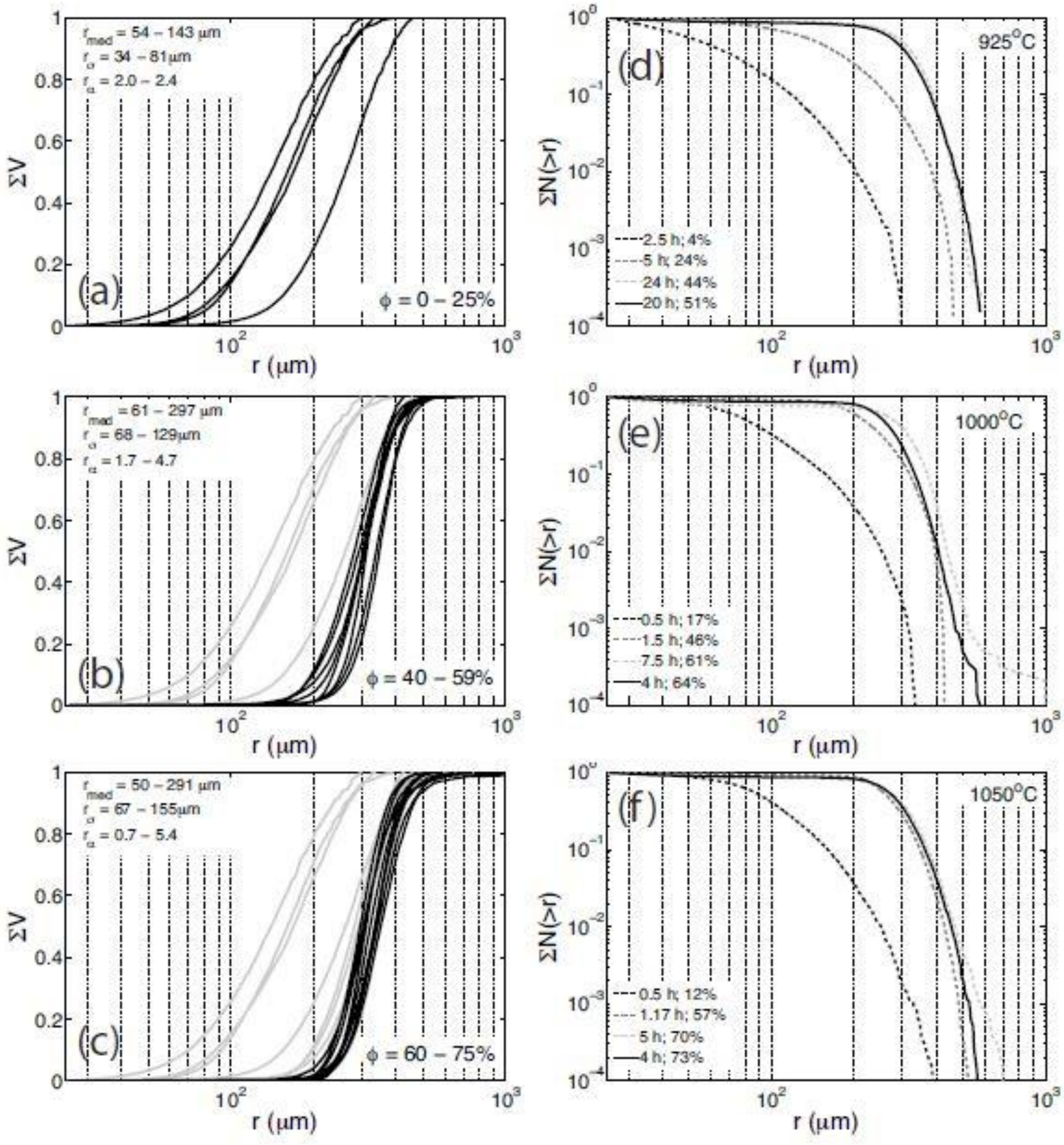

**Figure 4.** Cumulative bubble number fractions ($\Sigma N( >r)$) *vs*. bubble radius ($r$) for plateau samples from each $T$-suite (solid black lines in Fig. 3d,e,f) and corresponding XCT images of foamed cores. Each BSD curve features a horizontal plateau defined by smaller bubbles (< 200 μm) from which the curves decrease steeply to the maximum observed bubble sizes (500-600 μm). The steep negative slopes of the curves are nearly identical but represent diverse temperatures (900-1100°C), dwell times (1-20 h) and porosities (43-76%). XCT images of cores are taken at the same scale and illustrate the overall increase in bubble content of plateau samples with increasing $T$. Scale bars are 4 mm.

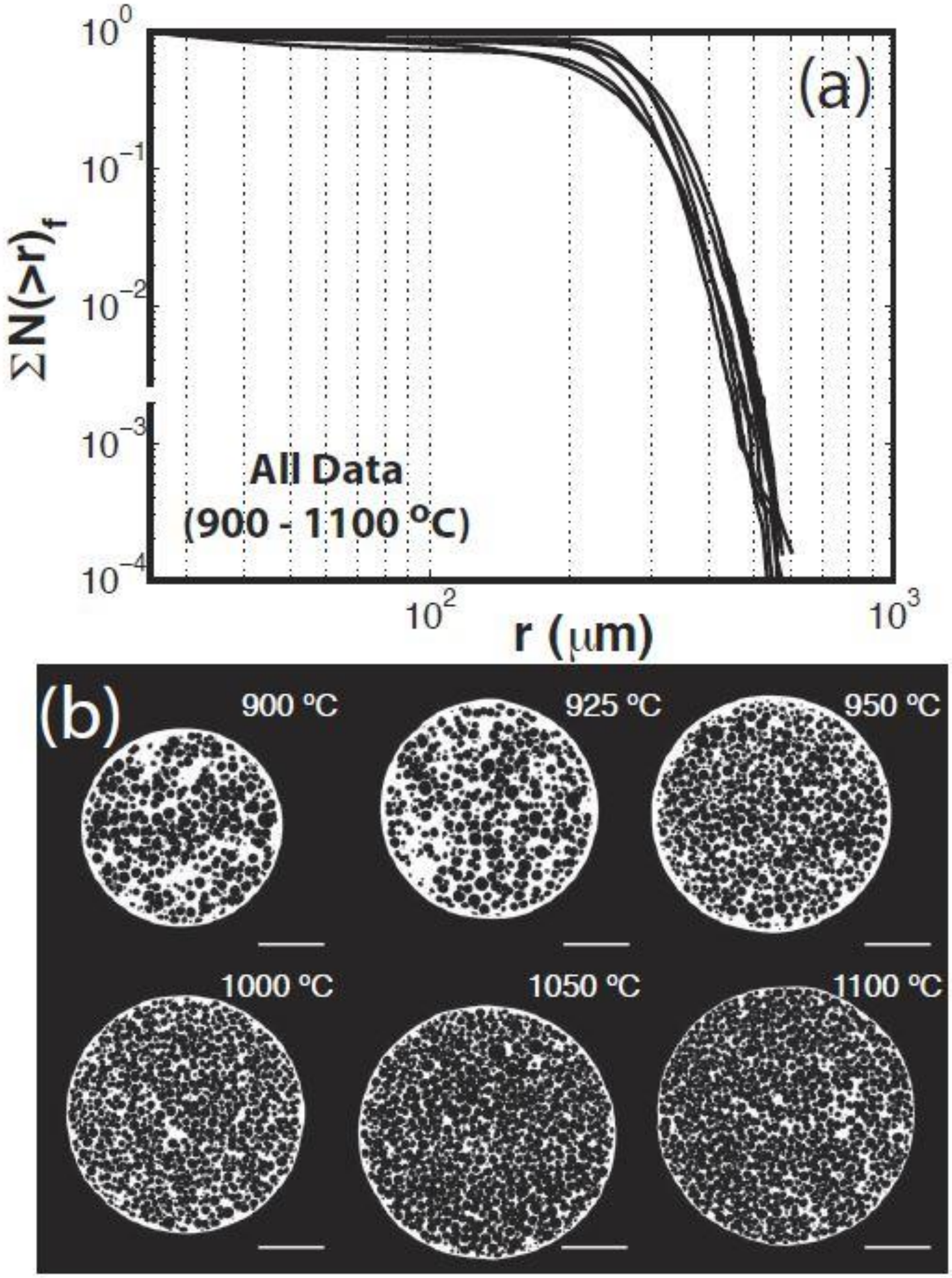

**Figure 5.** Thermodynamic description of vesiculation processes. (a) Experimental data shown as equilibrium constant (ln $K_{H2O}$) for $H_2O$ fluid in equilibrium with the melt *vs*. 1000/T (K). Oversaturated (non-equilibrium) samples are shown as open circles. Plateau samples from each T-suite (closed symbols) define chemical equilibrium and are used to estimate the enthalpy (ΔH°) and entropy (ΔS°) of the $H_2O$-melt equilibrium [*Ryan et al.*, 2015]. (b) Experimental data shown as calculated chemical affinity (*A*) for $H_2O$ exsolution *vs*. mole fraction of residual $H_2O$ dissolved in the melt (ln $X_{H2O}$). Initial sample cores are denoted by crossed circles. Samples quenched prior to reaching equilibrium are open symbols; samples at equilibrium (i.e. plateau samples) are shown as solid symbols. Model lines with slopes of 2 map the relationship between *A* and ln $X_{H2O}$ as a function of *T* (°C). Equilibrium (*A*=0) is denoted by the horizontal line and defines the transition from $H_2O$ oversaturation where vesiculation operates to $H_2O$ undersaturation where the melt would resorb $H_2O$.

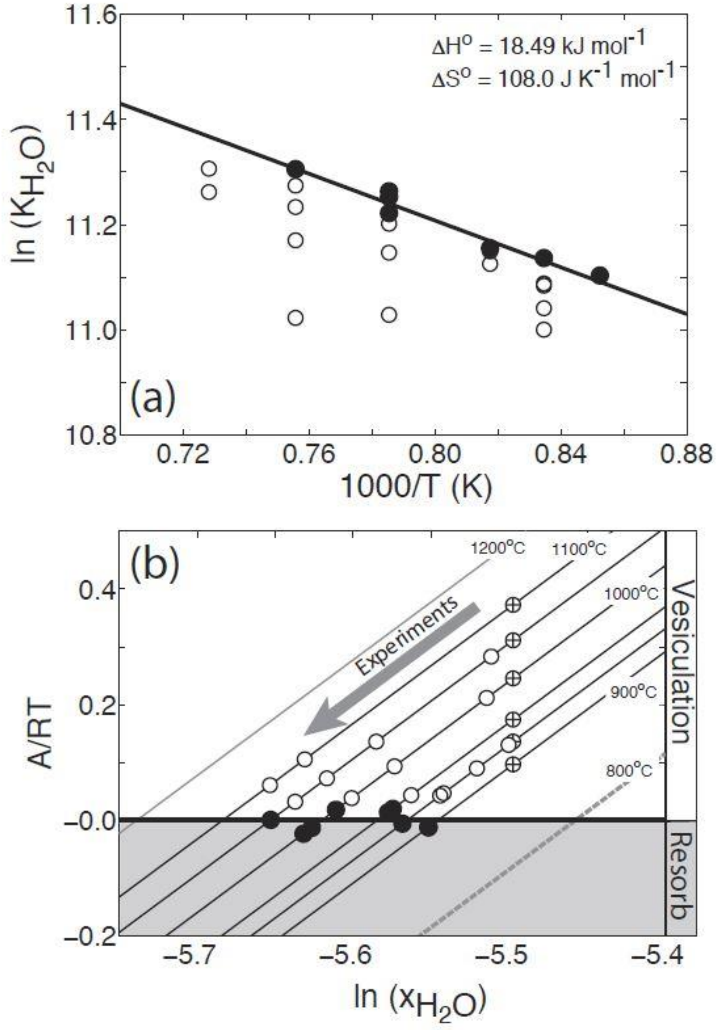

**Figure 6.** Rate of change in sample volume with temperature and viscosity. (a) Rate of sample volume increase for plateau samples plotted *vs*. 1000/T (K) (Table 3). The activation energy of vesiculation estimated from the slope of the model line is 269 kJ/mol. (b) Rate of volume change for plateau samples plotted *vs.* viscosity (log η; see Table 3). Values of ϕ shown in brackets. Increasing melt viscosity causes a decrease in rate of vesiculation. Supporting Information Text S3 provides additional analysis of the activation energies implied by these data.

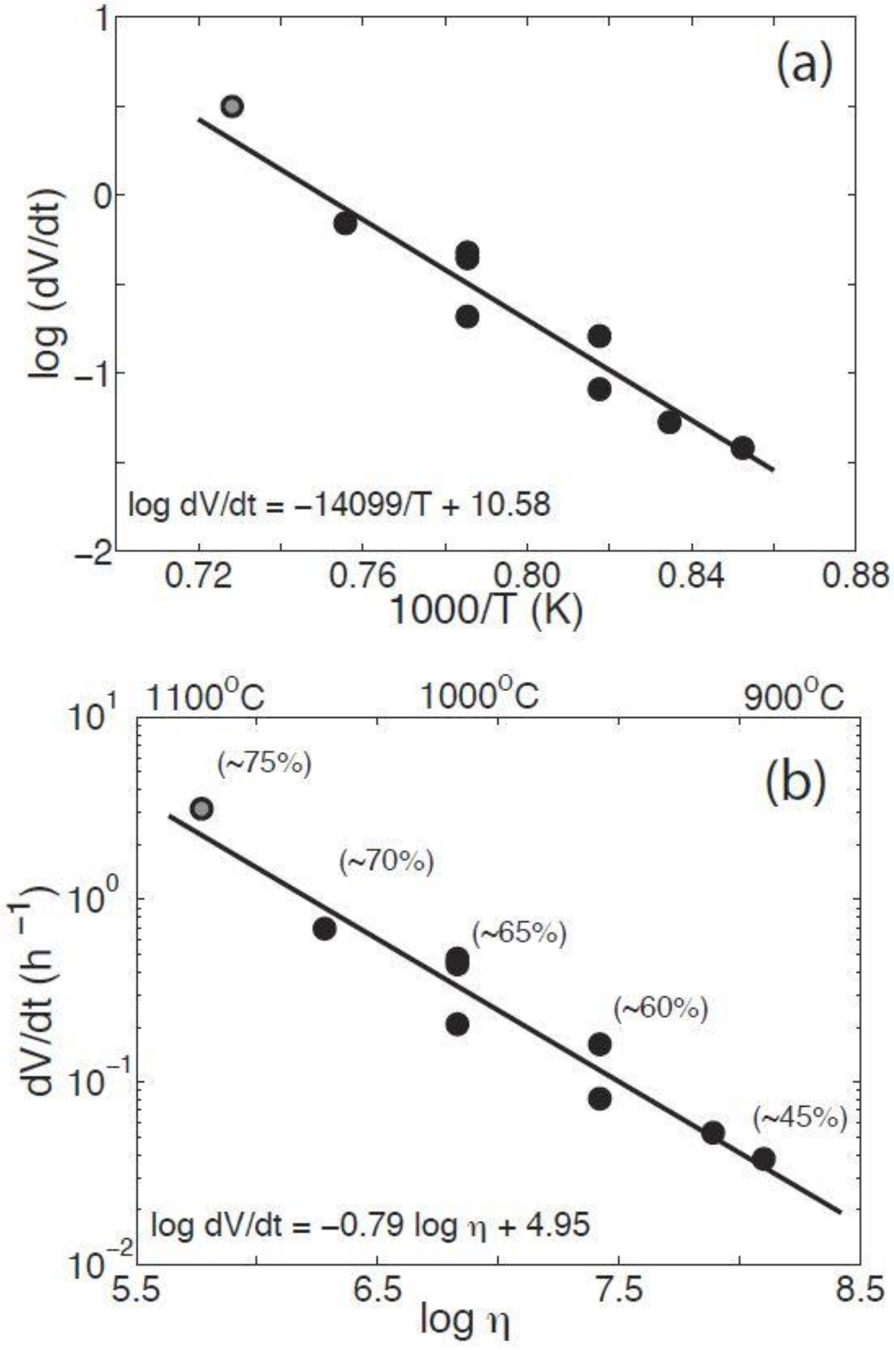

**Figure 7**. Time-dependent model for predicting vesiculation in rhyolitic melts. (a) A model for predicting vesiculation in rhyolitic melt as a function of time, melt viscosity, and affinity (Eq. 2) is calibrated against the experimental dataset. Model curves are shown for each isothermal temperature suite (symbols as in Fig. 2b) and feature a steep initial curve (proportional to viscosity) followed by a plateau (proportional to affinity). Error bars approximate the experimental uncertainty and are inversely proportional to magnitude of porosity. (b) Predicted *vs*. observed values of porosity. Agreement is greatest where ϕ> 40%. Data that lie off the 1:1 line have the largest uncertainties or reflect the steep slope of model curves at exceedingly short times (see text). (c) The optimal model parameters α and γ (closed symbol) are plotted on the contoured solution surface; the covariance ellipses for 3σ confidence limits are bounded by dashed box.

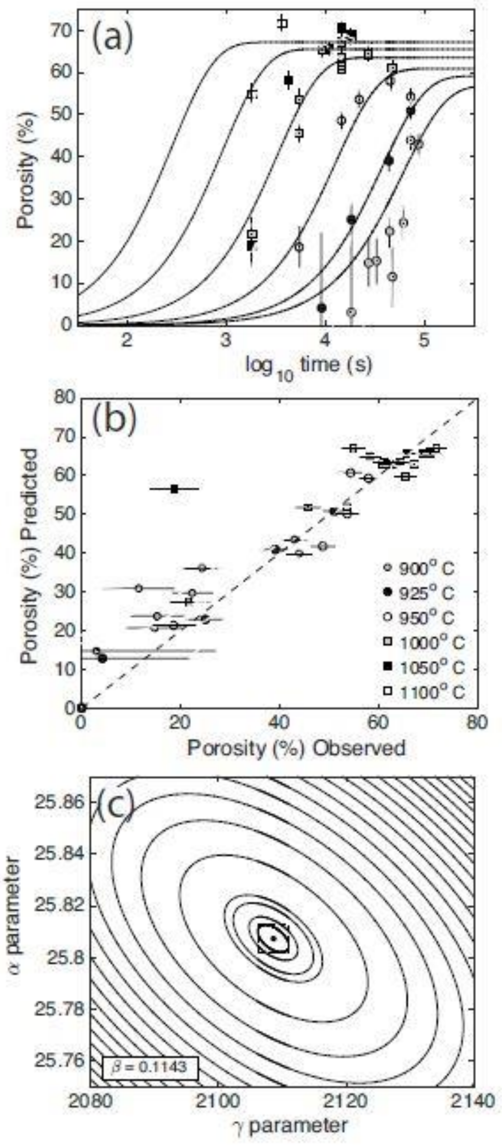

**Figure 8**. Time-dependent model for vesiculation applied to experimental dataset of Bagdassarov et al. [1996]. (a) Predictive model applied to their 805°C (grey symbols) and 883°C (black symbols) datasets and plotted as the volume of gas relative to the volume of melt ($V_{gas}/V_{melt}$) *vs*. time; the two model lines for each temperature represent a 10% variation in assumed volatile content (see text). (b) Model applied to all datasets (665-916°C) in Bagdassarov et al. [1996] plotted as log($V_{gas}/V_{melt}$) *vs*. log($t$) showing linear increase in porosity with time until saturation is reached. Inset shows trend lines based on digitization of original published datasets; original data for 805°C and 883°C experiments (cf. Fig 8a) are denoted as solid black curves.

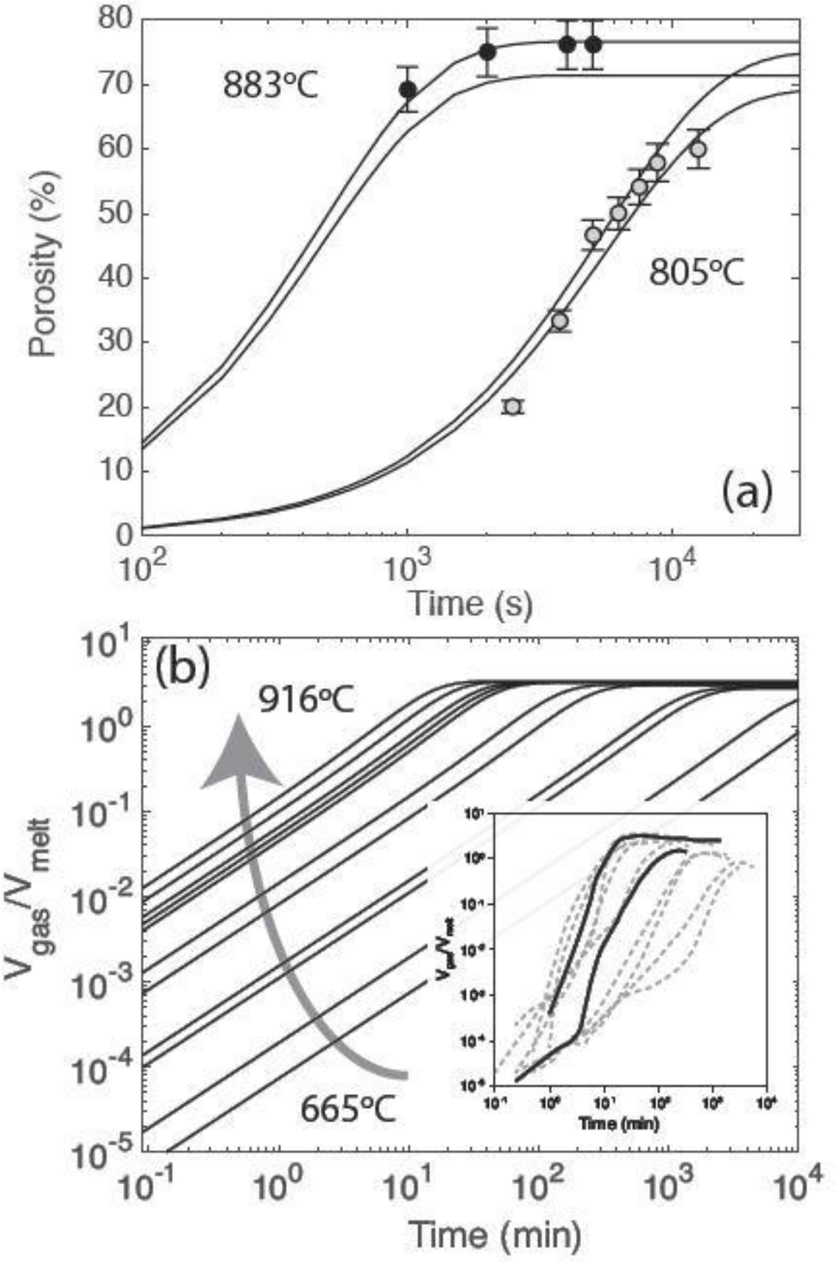

**Figure 9**. Regime diagrams for vesiculation of rhyolite. (a) Summary of model implications illustrated as porosity ($\phi$) plotted against dimensionless time ($t_D = t/\tau_\eta$) for different degrees of oversaturation represented by $A$ (kJ). With increasing $A$, the melt vesiculates more rapidly before reaching a higher final porosity at $t_D \approx 10^{7.5}$. For example, the grey dashed vertical lines denote the corresponding times for a rhyolite melt having a viscosity of $10^8$ Pa s. (b) Model implications illustrated as dimensionless vesiculation rate ($R_D$) plotted *vs*. dimensionless time. Model values of $R_D$ decay exponentially with increasing $t_D$; at $10^{6.4}$ the vesiculation rate is reduced by 50%. Grey vertical lines as in (a).

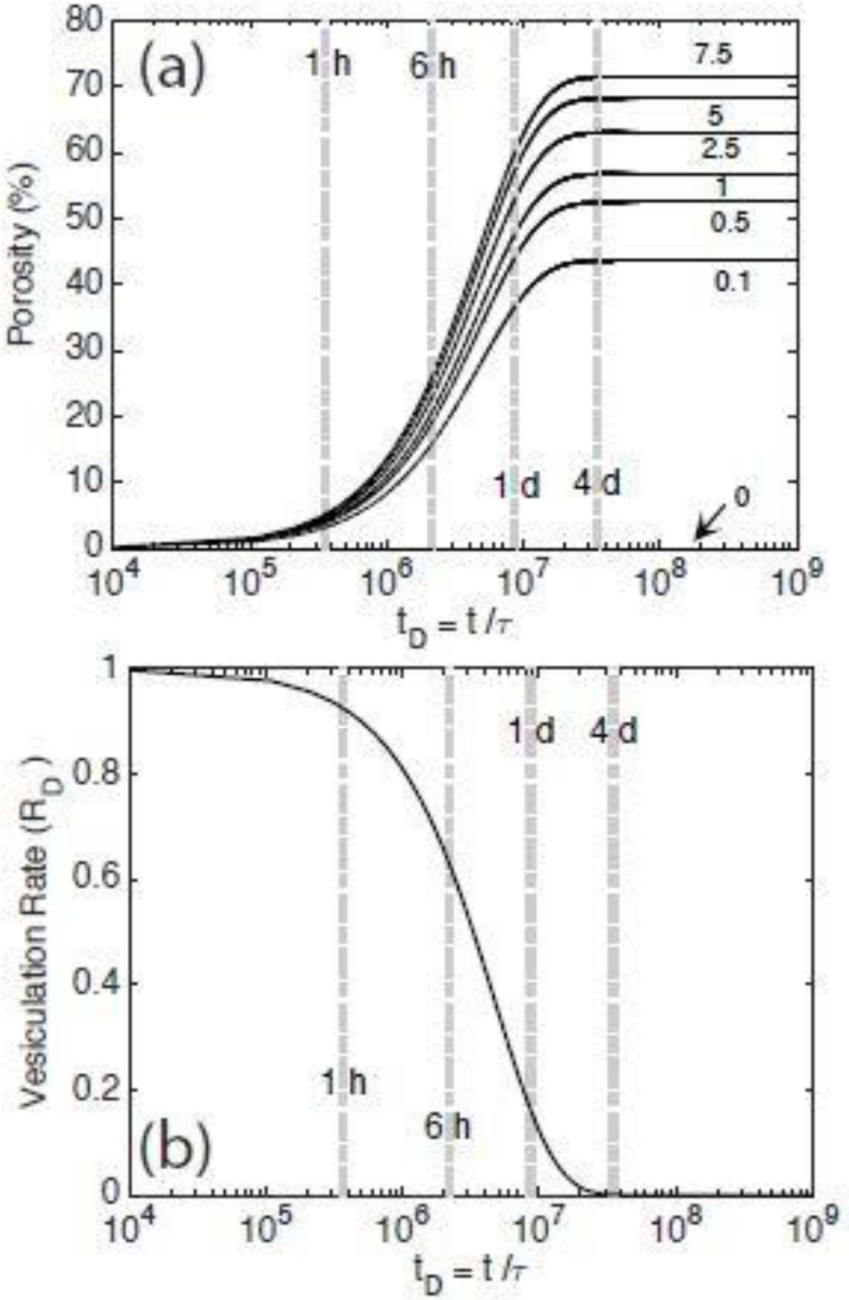

**Figure 10.** Porosity and transport properties resulting from the isothermal ascent and vesiculation of hydrous rhyolite magma as a function of magma ascent rate(see text for initial magma conditions). The equilibrium vesiculation path is modelled using the program rhyolite-MELTS [*Gualda et al.,* 2012], melt viscosity is calculated with the GRD model [*Giordano et al.,* 2008], and bulk viscosity of the vesiculated magma is approximated using the model of Quane et al. [2009]. (a) The extent of vesiculation in the ascending magma (i.e. porosity) as calculated with Eq. 2 is plotted as a function of depth for a variety of magma rise rates (m $s^{-1}$; labelled curves). Fluid saturation occurs at ~ 1450 m depth after which vesiculation begins. At low magma ascent rates (< 0.001 m $s^{-1}$) the extent of vesiculation predicted by our model (Eq. 2) is equal to the equilibrium exsolution path (heavy line). As magma rise rate increases the departure from this end-member increases. The shaded fields denote rates attending slow extrusion of rhyolite lava and domes (D) and the range of "fast" rise rates estimated for the Chaiten (Ch) eruption (see text). (b) The same model data sets as above expressed as the bulk viscosity of the magma due to vesiculation, modelled using the empirical equation of Quane et al. [2009]. The increase in melt viscosity with loss of $H_2O$ (heavy line on left) during ascent is moderated by the presence of bubbles, resulting in deviation of model curves from that of the melt viscosity.